Title

Epitaxial antiperovskite/perovskite heterostructures for materials design

Journal

Science Advances, 6(30)

ISSN

2375-2548

Authors

Quintela, Camilo X

Song, Kyung

Shao, Ding-Fu

et al.

Publication Date

2020-07-24

DOI

10.1126/sciadv.aba4017

MATERIALS SCIENCE

Epitaxial antiperovskite/perovskite heterostructures for materials design

Camilo X. Quintela[1], Kyung Song[2], Ding-Fu Shao[3], Lin Xie[4], Tianxiang Nan[1], Tula R. Paudel[3], Neil Campbell[5], Xiaoqing Pan[6], Thomas Tybell[7], Mark S. Rzchowski[5], Evgeny Y. Tsymbal[3], Si-Young Choi[8]*, Chang-Beom Eom[1]*

Engineered heterostructures formed by complex oxide materials are a rich source of emergent phenomena and technological applications. In the quest for new functionality, a vastly unexplored avenue is interfacing oxide perovskites with materials having dissimilar crystallochemical properties. Here, we propose a unique class of heterointerfaces based on nitride antiperovskite and oxide perovskite materials as a previously unidentified direction for materials design. We demonstrate the fabrication of atomically sharp interfaces between nitride antiperovskite Mn_3GaN and oxide perovskites $(La_{0.3}Sr_{0.7})(Al_{0.65}Ta_{0.35})O_3$ and $SrTiO_3$. Using atomic-resolution imaging/spectroscopic techniques and first-principles calculations, we determine the atomic-scale structure, composition, and bonding at the interface. The epitaxial antiperovskite/perovskite heterointerface is mediated by a coherent interfacial monolayer that interpolates between the two antistructures. We anticipate our results to be an important step for the development of functional antiperovskite/perovskite heterostructures, combining their unique characteristics such as topological properties for ultralow-power applications.

INTRODUCTION

Complex oxide materials and in particular heterostructures formed from them are a rich source of emergent phenomena and technological applications (*1*–*3*). Interfacing oxide perovskites with materials having dissimilar crystallochemical properties and functionalities (*4*) are likely to vastly expand the range of interfacial phenomena and applications. However, stabilizing such heterostructures with the chemical and structural quality required to promote the desired functionality is challenging when the constituting materials are non-isostructural, having large geometrical and chemical strains (*5*, *6*). We propose a unique class of heterointerfaces based on nitride antiperovskite and oxide perovskite materials as a new direction for materials design.

Antiperovskite materials are intermetallic compounds with perovskite crystal structure (space group $Pm\bar{3}m$, no. 221) but with anion and cation positions interchanged in the unit cell (*7*). Like their oxide perovskite counterparts, antiperovskite materials show a variety of tunable physical properties, including superconductivity, itinerant antiferromagnetism, giant magnetoresistance, large magnetovolume effects, and topological electronic behavior (*8*–*15*). Among antiperovskite materials, transition metal (TM)–based nitride compounds (M_3XN; M: TM; X: metallic or semiconducting element) are particularly interesting as their physical behaviors are remarkably sensitive to external perturbations such as magnetic fields, temperature, or pressure (*14*–*20*). This is mainly due to the strong spin-lattice coupling characteristic of M_3XN compounds. With such a correlated physical background, the development of epitaxial M_3XN heterostructures provides an ideal platform for tuning the properties of M_3XN with the proper choice of materials and design. In this context, ABO_3 oxide perovskites are unrivaled material systems to interface with M_3XN nitride antiperovskites as both compounds have analogous perovskite-type crystal structure with comparable lattice constants, affording good epitaxial match along any common crystallographic direction, which should thus promote epitaxial growth. This enables the use of strain engineering to tune the behavior of M_3XN materials. In addition, the wide variety of physical properties of ABO_3 compounds can be used as external triggers to tune the functionality of antiperovskite materials, allowing the development of multifunctional artificial materials and devices, such as recently proposed for heterostructures between Mn_3GaN and oxide ferroelectric and piezoelectric perovskites (*16*–*19*).

To exploit this potential, it is first necessary to understand at the atomic level the interfacial structure and chemistry between nitride antiperovskite and oxide perovskite materials to promote a bridging structure allowing for epitaxy. From the crystallographic perspective, the atomic configuration at the interface between these two antistructures is not obvious. As illustrated in Fig. 1A, M_3XN antiperovskite and ABO_3 perovskite compounds show reversed anion and cation positions in the unit cell. This distinctive difference leads to different considerations for interfaces between M_3XN and ABO_3 materials than that between two perovskite or two antiperovskite materials (Fig. 1B). The ABO_3 perovskite structure can be described as alternating mixed cation-anion AO and BO_2 layers along the $[001]_{perovskite}$ ($[001]_P$) direction of the unit cell, and only two trivial interfacial configurations are physically stable for interfaces formed between two different ABO_3 and $A'B'O_3$ compounds: $A'O/BO_2$ and $B'O_2/AO$ (Fig. 1C). Using the same analogy, nitride M_3XN antiperovskites can be viewed as a stacking of alternating MX and M_2N layers along the $[001]_P$ direction. As illustrated in Fig. 1D, the number of hypothetical simplest

[1]Department of Materials Science and Engineering, University of Wisconsin-Madison, Madison, WI 53706, USA. [2]Department of Materials Modeling and Characterization, KIMS, Changwon 51508, South Korea. [3]Department of Physics and Astronomy and Nebraska Center for Materials and Nanoscience, University of Nebraska, Lincoln, NE 68588, USA. [4]National Laboratory of Solid State Microstructures and College of Engineering and Applied Sciences, Nanjing University, Nanjing, Jiangsu 210093, People's Republic of China. [5]Department of Physics, University of Wisconsin-Madison, Madison, WI 53706, USA. [6]Department of Materials Science and Engineering and Department of Physics and Astronomy, University of California-Irvine, Irvine, CA 92697, USA. [7]Department of Electronic Systems, Norwegian University of Science and Technology, Trondheim 7491, Norway. [8]Department of Materials Science and Engineering, POSTECH, Pohang 37673, South Korea.
*Corresponding author. Email: eom@engr.wisc.edu (C.-B.E.); youngchoi@postech.ac.kr (S.-Y.C.)

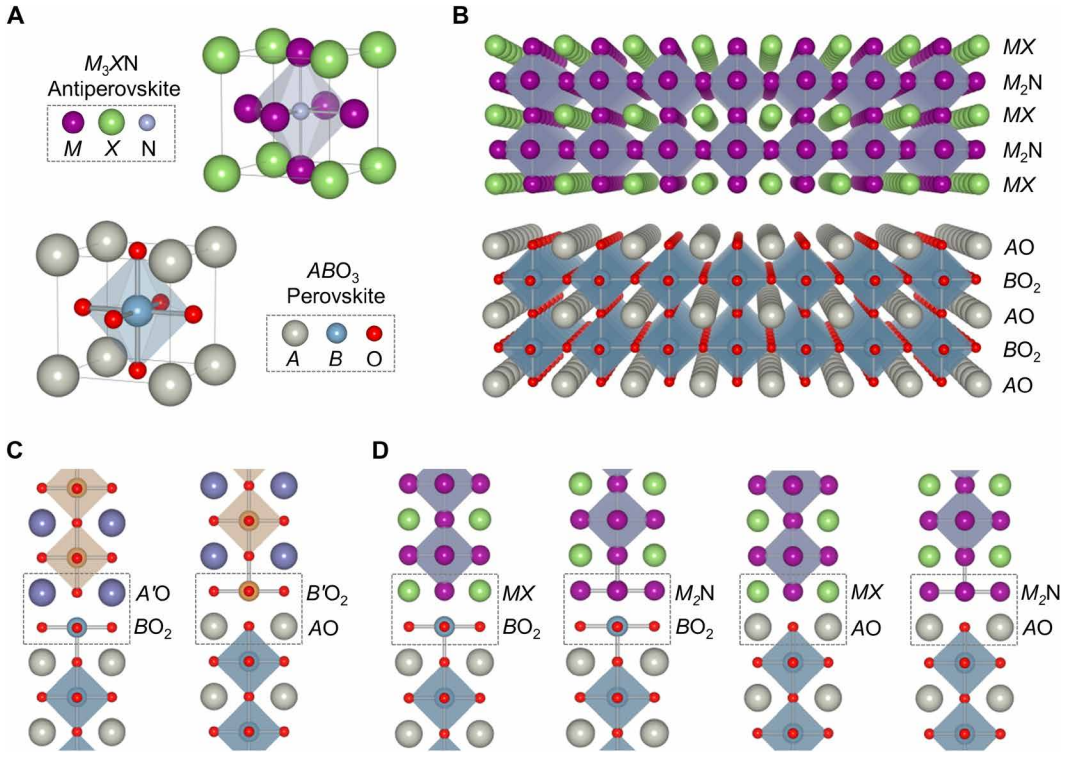

Fig. 1. Schematic representation of the crystal structures of M_3XN nitride antiperovskite and ABO_3 oxide perovskite compounds and their interfaces. (**A**) M_3XN and ABO_3 ideal unit cells showing their geometrically analogous crystal structures and reversed anion (N and O) and cation (*M* and *B*) positions in the unit cell. (**B**) M_3XN and ABO_3 slabs represented as a stacking of alternating *AO* and BO_2 and M_2N and *MX* planes, respectively. (**C**) Representation of the two proven atomically sharp interfacial configurations (*A'O*:BO_2 and $B'O_2$:*AO*) between two different oxide perovskite compounds ABO_3 and $A'B'O_3$. (**D**) Representation of the four possible atomically abrupt interfacial configurations (*MX*:BO_2, M_2N:BO_2, *MX*:*AO*, and M_2N:*AO*) between ABO_3 and M_3XN compounds, depending on the ABO_3 termination layer.

possible interfacial configurations between M_3XN antiperovskite and ABO_3 perovskite materials doubles to four depending on the termination of the ABO_3 perovskite: M_2N/BO_2, MX/BO_2, M_2N/AO, and MX/AO. However, a fundamental subsequent consideration is the chemical bonding at the interface between nitride antiperovskite and oxide perovskite materials. Contrary to oxide perovskites, which have predominantly ionic bonding, nitride antiperovskites generally show metallic/covalent chemical bonding. In this context, developing a strategy to properly interface nitride antiperovskites with oxide perovskite materials can facilitate the emergence of interfacial hybridization interactions and hence interfacial properties and functionalities not achievable in more conventional oxide/oxide interfaces, opening a new path in the search for emergent behavior linked to interfacial phenomena (*4*).

Sparked by the quest for fundamental understanding of the nitride antiperovskite/oxide perovskite interface, we fabricated high-quality epitaxial Mn_3GaN films on (001)-oriented $(La_{0.3}Sr_{0.7})(Al_{0.65}Ta_{0.35})O_3$ (LSAT) and $SrTiO_3$ single-crystal substrates as paradigms of M_3XN/ABO_3 interfaces. Using a combination atomic-resolution scanning transmission electron microscopy (STEM), electron energy-loss spectroscopy (EELS), energy-dispersive x-ray spectroscopy (EDS) techniques, and density functional theory study, we studied the interfacial structure of Mn_3GaN/LSAT and $Mn_3GaN/SrTiO_3$ on an atomic scale. We investigated both the stability and the mechanism of nucleation of the observed interface using first principles calculations. For simplicity, the manuscript focuses on the Mn_3GaN/LSAT interface. Additional information, including experimental data regarding the $Mn_3GaN/SrTiO_3$ interface and materials and methods, is presented in the Supplementary Materials.

RESULTS

Figure 2 summarizes the x-ray diffraction (XRD) structural characterization for a 60-nm-thick Mn_3GaN film grown on a (001) LSAT substrate. The epitaxial growth and single-phase structure of the films were monitored using in situ reflection high-energy electron diffraction (RHEED) and confirmed through symmetric θ-2θ XRD measurements by the observation of only the (00*l*) reflections (Fig. 2A). In Fig. 2B, a representative θ-2θ XRD scan taken around the (002) LSAT substrate peak is shown. The presence of Kiessig fringes surrounding the Mn_3GaN (002) reflection indicates the high crystalline quality of the film and a pristine interface, corroborated by the narrow 0.035° full width at half maximum (FWHM) value of the rocking curve for Mn_3GaN (002) (Fig. 2C). Decreasing film thickness results in an improvement of the crystallinity, reaching films with FWHM values as low as 0.023°. An in-plane cube-on-cube epitaxial relationship between Mn_3GaN and substrate was confirmed by off-axis azimuthal ϕ-scan around the (022) reflection (Fig. 2D). From x-ray reciprocal space mapping (RSM) measurements centered in the asymmetrical (−113) LSAT peak (Fig. 2E), the out-of-plane ($a_\perp$) and in-plane ($a_{||}$) lattice constants were determined at $a_\perp = 3.90 \pm 0.01$ Å and $a_{||} = 3.92 \pm 0.01$ Å, close to the bulk lattice constant of $a = 3.898$ Å (*21*).

To investigate the structure and chemical composition of the Mn_3GaN/LSAT interface, we used a combination of atomic-resolution

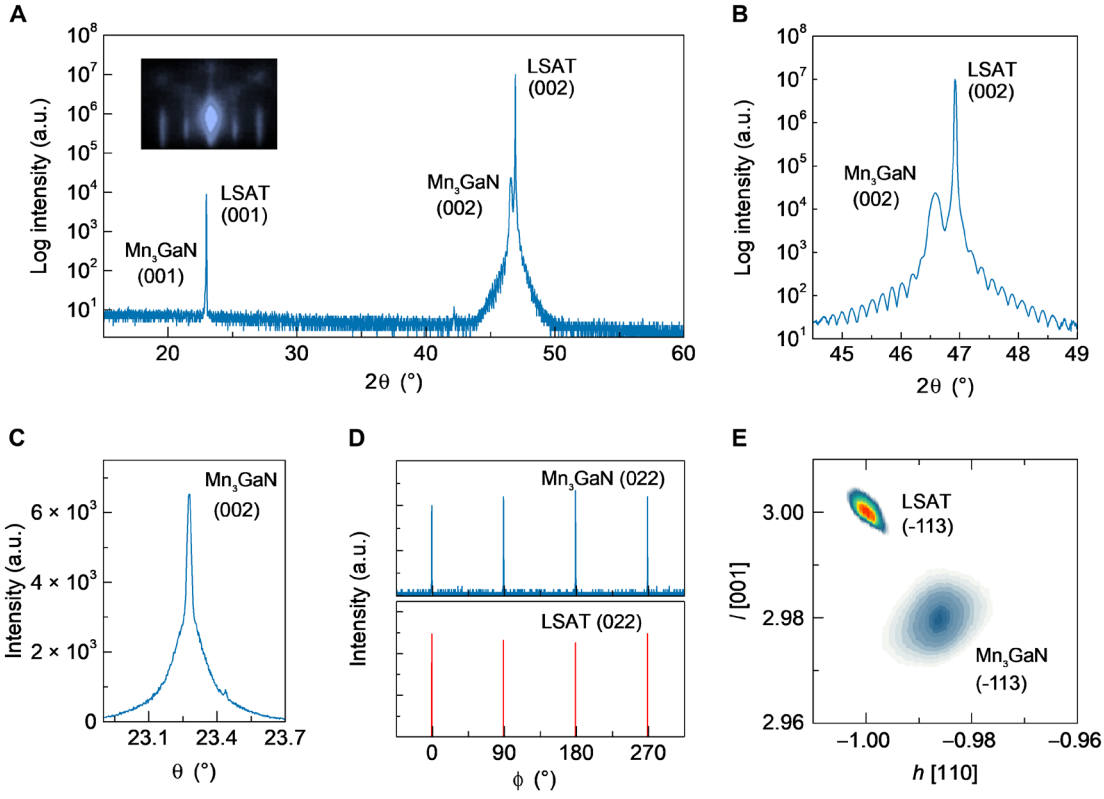

Fig. 2. XRD structural characterization of a 60-nm-thick Mn_3GaN grown on a (001)-oriented LSAT substrate. (**A**) Wide-angle θ-2θ spectrum only shows the (00*l*) reflections of the LSAT substrate and the Mn_3GaN film, demonstrating that the film is (001)-oriented and single phase. Inset shows registered reflection high-energy electron diffraction (RHEED) pattern of the specular diffraction spot after growth. (**B**) Short-range θ-2θ scan around the (002) diffraction peak of the Mn_3GaN film showing Kiessig fringes, indicating pristine interfaces and high crystalline quality of the film. (**C**) Rocking curve of the (002) Mn_3GaN peak. (**D**) Three hundred sixty–degree ϕ-scans around the Mn_3GaN and LSAT (022) peaks demonstrate cube-on-cube epitaxial relationship. (**E**) Reciprocal space mapping (RSM) around the LSAT (-113) reciprocal lattice point shows that the Mn_3GaN is strain relaxed. a.u., arbitrary units.

STEM, EELS, and EDS techniques. For additional analyses, including data for the $Mn_3GaN/SrTiO_3$ interface, please see the Supplementary Materials. In Fig. 3A, we show an atomic-resolution high-angle annular dark-field (HAADF)–STEM image taken along the [100] zone axis of LSAT. The image displays an atomically sharp interface and further corroborates the high crystalline quality of the films. In Fig. 3B, a magnified HAADF-STEM image close to the epitaxial Mn_3GaN/LSAT interface is shown, overlaid with the cation positions, as determined by this study. The atomic-resolution EDS and EELS analyses (figs. S1 and S2) and HAADF-STEM intensity profiles (Fig. 3C) demonstrate that the LSAT substrate termination is $(Al_{0.65}Ta_{0.35})O_2$ (BO_2 termination) and thus implies that the Mn_3GaN termination at the interface is expected to be Mn_2N. However, we noticed that the first Mn_3GaN interfacial monolayer (labeled as layer 1 in Fig. 3C) exhibits a pattern of alternating bright and dark spots, indicative of compositional and/or structural reconfigurations at the interface.

We performed atomic-resolution EDS and EELS measurements to determine the atomic composition of the first monolayer above the LSAT substrate (see figs. S1 and S2). The Mn intensity measured at the first Mn_2N layer at the interface was found to be notably lower compared to Mn_2N layers far from the interface. This difference in Mn intensity, together with the observed alternating pattern of bright and dark spots in the HAADF-STEM image, points to a lower relative Mn concentration in every other atomic position (dark-contrast spots) along the [100] direction in the interfacial monolayer. We quantified the Mn concentration at the interfacial monolayer with HAADF-STEM image simulations (xHREM software, HREM Research Inc., Japan), changing the Mn occupancy for the best fit (fig. S3). The simulations are compatible with an approximately 80% Mn deficiency in the atomic positions, corresponding to a darker contrast in the HAADF-STEM data. Thus, the combination of simulations and structural and chemical analyses indicates that the transition from the LSAT substrate to the Mn_3GaN film is mediated by a sharp interfacial Mn_xN monolayer with $x \sim 1.2$.

To unequivocally determine the atomic structure of the Mn_xN interfacial monolayer, we performed additional STEM and EDS analyses along the [110] zone axis (fig. S4). In Fig. 4, we show the schematic of the proposed Mn_3GaN/LSAT interface based on analyses along the [100] and [110] zone axes. This model is also consistent with STEM analyses that we performed in epitaxial Mn_3GaN films grown on (001)-oriented $SrTiO_3$ (see the Supplementary Materials). Indistinguishable projections of the Mn_xN monolayer along the [100] and [010] directions indicate that the ordering of Mn and N atoms constitutes a two-dimensional periodic structure with C_4 rotational symmetry. Considering $x = 1$ for simplicity, the ideal MnN monolayer would be arranged as depicted in Fig. 4 (B and C), with the N atoms located above (Al/Ta) atoms of LSAT and the Mn atoms over the interstice of the $(Al/Ta)O_2$ layer of LSAT. The illustration shows that the ideal MnN interfacial monolayer has an analogous structure

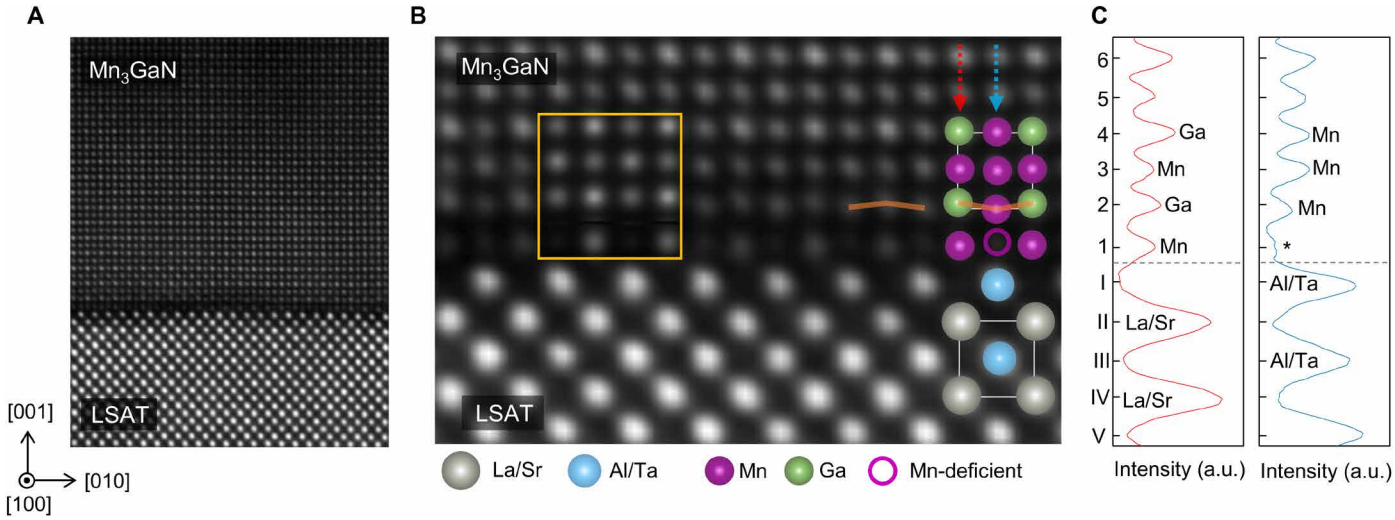

Fig. 3. HAADF-STEM characterization of the Mn_3GaN/LSAT heterointerface. (**A**) High-angle annular dark-field (HAADF)–STEM imaging of the Mn_3GaN/LSAT heterostructure taken along the [100] zone axes of LSAT. (**B**) Magnified HAADF-STEM imaging overlaid with the cation positions and simulated image of the interface (yellow square). Orange lines are a guide to the eyes, showing buckling of the Mn and Ga atoms at the second row. (**C**) Integrated HAADF-STEM intensity line profile along two adjacent atomic columns [out-of-plane direction, represented by arrows in (B)]. Ordinate *y* axis shows the layer's number, denoted by roman numerals for LSAT and Arabic numerals for Mn_3GaN. Since the HAADF-STEM intensity is proportional to Z^2 (*Z*, atomic number), Ga atoms show higher intensity than Mn atoms. The * symbol indicates Mn deficiency.

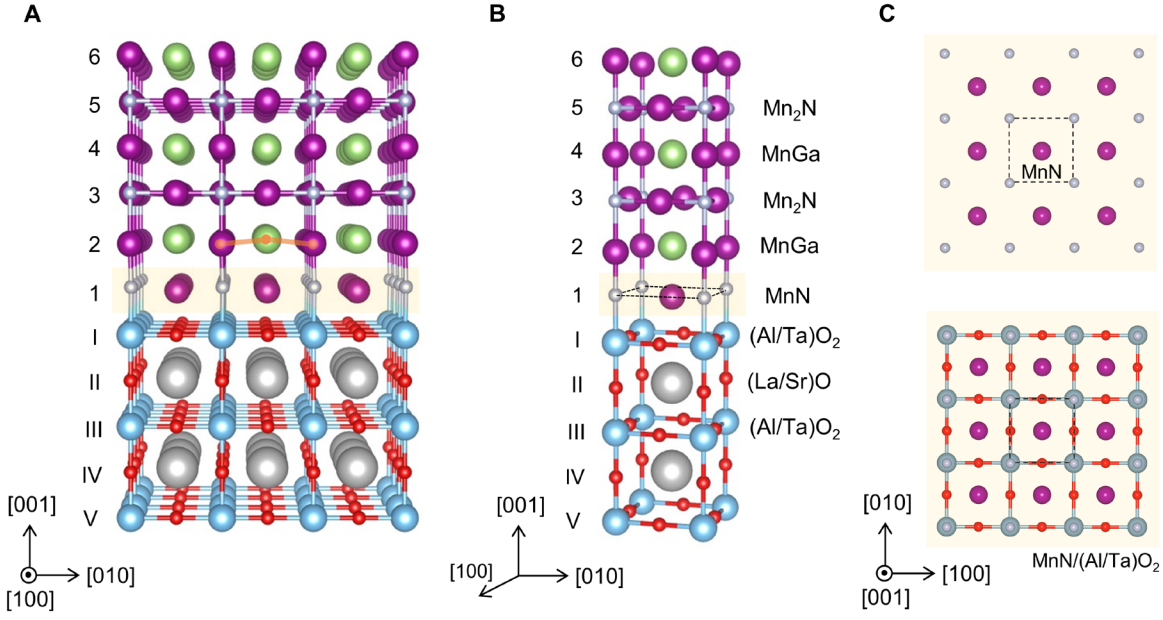

Fig. 4. Illustration of the Mn_3GaN/LSAT heterointerface based on our experimental results. (**A**) Schematic [100] perspective view of the Mn_3GaN/LSAT heterointerface. Orange line in layer 2 is a guide to the eyes, showing buckling of the Mn and Ga atoms. (**B**) Representation of the Mn_3GaN/LSAT heterointerface as a stacking of atomic unit cell planes. (**C**) [001] projections of the MnN interfacial layer (top image) and MnN layer overlaid with the $(Al/Ta)O_2$ LSAT termination layer (bottom image). Dashed square represents the interfacial MnN unit cell.

as a perovskite *AO* layer, with *A* being Mn and N being O. Moving away from the interface, a MnGa puckered layer is observed occurring on top of the MnN interfacial layer (Fig. 3B), with the Mn cations displaced toward the interface. A gradual decrease of the interplanar distances along the [001] direction within the first five layers of above the interface is also apparent. Above the fifth layer, the interplanar distance reaches the bulk value.

We performed first-principles calculations to study the stability of the interfacial model derived from the atomic-resolution experiments. Because of the complex crystal structure of LSAT, AlO_2-terminated $LaAlO_3$ was used to mimic BO_2-terminated LSAT. $Mn_3GaN/LaAlO_3$ with two different interfaces, MnN/AlO_2 and Mn_2N/AlO_2, were simulated, as shown in Fig. 5A. Specifically, their formation energies ΔE were calculated to test for stability. As shown in Table 1, the calculated

results indicate that both interfaces have negative ΔE, which implies that both are energetically stable. However, $\Delta E = -2.265$ eV for the Mn_2N interface is appreciably lower than that of the observed MnN interface, $\Delta E = -0.058$ eV. The lower ΔE for the Mn_2N interface can be understood from the chemical bonding at the interface. As shown in Fig. 5 (B and C), the charge density between Mn and O (or N) at the MnN interface is notably smaller than that of the Mn_2N interface, corresponding to a stronger Mn—O and Mn—N bonding at a Mn_2N interface, thus resulting in a more cohesive and energetically stable interface.

The apparent discrepancy between the interfacial models derived from the experimental and theoretical studies can be explained by considering the onset of Mn_3GaN growth in the presence of an energy barrier, preventing the system from relaxing from the local to the global energy minimum. To explore this hypothesis, the formation energies for $Mn/LaAlO_3$ were calculated using two different Mn configurations, Mn(1) and Mn(2), as shown in fig. S10. Mn(1) and Mn(2) correspond to the positions of Mn in the MnN and Mn_2N interfaces, respectively, as described in Fig. 5D. The $Mn/LaAlO_3$ supercell with the Mn atom located in the Mn(1) site had a lower energy than that of the Mn atom at the Mn(2) position (Table 1). An analogous behavior was observed by calculations using the nonpolar $SrTiO_3$ surface, which indicates that the Mn(1) site is the most energetically favorable position for Mn on both polar and nonpolar ABO_3 perovskite surfaces. While Mn(1) is surrounded by four O^{2-} anions, in the vicinity of Mn(2), there is one O^{2-} and two B cations. The strong local coulomb repulsion between Mn(2) and the B cations accounts for the higher formation energy of the $Mn(2)/ABO_3$ supercells. In addition, the more positive the B cation, the higher energy of the Mn(2) site. As shown in Table 1, the calculated energy difference between $Mn(1)/SrTiO_3$ and $Mn(2)/SrTiO_3$ (0.452 eV) is larger than that of $Mn(1)/LaAlO_3$ and $Mn(2)/LaAlO_3$ (0.155 eV), mainly due to Ti^{4+} being more positive than Al^{3+}. Thus, the Mn(2) site in the $Mn(2)/LSAT$ system will hence be more unstable because of the Ta^{5+} cations in the LSAT terminating layer.

Therefore, our combination of experimental and theoretical studies indicates that, during the initial growth of Mn_3GaN, Mn ions arriving at the B-terminated ABO_3 layer sit on the Mn(1) positions and then coordinate with N, forming a Mn_xN monolayer as determined by the STEM studies. This interfacial monolayer works as a structural bridge between the ABO_3 substrate and Mn_3GaN film and establishes heteroepitaxy between the two nonisostructural materials with different chemical composition and bonding. Moreover, the experimentally observed puckered GaMn layer can be related to the strong out-of-plane Ga—Mn bonding due to the strong charge density overlap between Mn in the first interfacial layer and Ga in layer 2 (Fig. 5B and fig. S11).

DISCUSSION

The realization of an atomically sharp bridging structure allowing an epitaxial interface structure and bonding between nitride antiperovskites and oxide perovskites manifests a critical step in the development of a new class of epitaxial heterostructures based on materials with dissimilar crystallochemical properties. The ability to engineer such novel heterointerfaces from chemically divergent constituents brings a new dimension to the mature field of complex oxides and provides a playground for the manipulation of the interfacial physical properties and the establishment of new states of matter. In particular, Mn-based nitride antiperovskites with noncollinear Γ^{5g} triangular antiferromagnetic structures are ideal systems to interface with piezoelectric or ferroelectric oxide compounds to induce piezomagnetic or magnetoelectric effects in the antiperovskite, as recently proposed theoretically (*16*–*19*) and demonstrated experimentally (*22*). In addition, materials showing geometrically frustrated antiferromagnetic spin structures are the source of intriguing physical

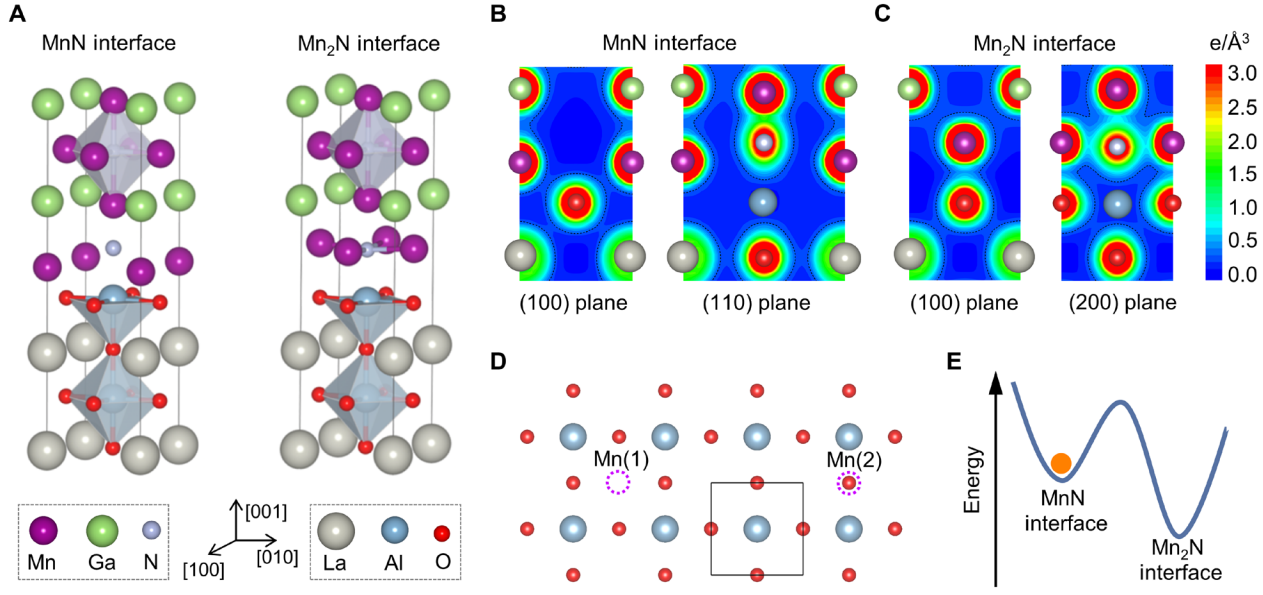

Fig. 5. Theoretical calculations for different interfacial configurations. (**A**) Sections of the relaxed $Mn_3GaN/LaAlO_3$ supercell with the MnN/AlO_2 interface and the Mn_2N/AlO_2 interface. (**B**) Charge density plots around the MnN interface in the (100) and (110) planes. (**C**) Charge density plots around the Mn_2N interface in the (100) and (200) planes. (**D**) Illustration of the two possible deposited positions of Mn atoms Mn(1) and Mn(2) (purple dashed circles) onto the AlO_2 plane. (**E**) Schematic diagram of energies of MnN interface and Mn_2N interface, showing that the MnN interface is in a local energy minimum.

Table 1. Formation energy for different interfacial configuration. Calculated formation energies ΔE of $Mn_3GaN/LaAlO_3$ for two interfacial configurations: MnN and Mn_2N. Calculated ΔE for Mn deposited in the Mn(1) and Mn(2) positions onto BO_2-terminated $LaAlO_3$ and $SrTiO_3$.

	$Mn_3GaN/LaAlO_3$ (MnN interface)	$Mn_3GaN/LaAlO_3$ (Mn_2N interface)	$Mn(1)/LaAlO_3$	$Mn(2)/LaAlO_3$	$Mn(1)/SrTiO_3$	$Mn(2)/SrTiO_3$
ΔE (eV/interface)	−0.058	−2.265	−0.980	−0.825	−1.698	−1.246

behavior, including large anomalous Hall (*23*, *24*) and Nernst effects, large magnetoresistance, spin transfer torque, and spin Hall effect (*25*–*28*). Given the potential of these materials for antiferromagnetic spintronics (*29*), the rational design of epitaxial heterostructures of Mn-based nitride antiperovskites and ABO_3 perovskites is of great importance for property tuning and functional device design. We expect our study to trigger the investigation and development of functional antiperovskite/perovskite heterostructures, opening a new and exciting avenue for materials design.

MATERIALS AND METHODS

Sample growth and x-ray characterization

Thin-film heterostructures were grown by DC reactive planar magnetron sputtering using a Mn_3Ga stoichiometric target (99.9% purity) at 50 W. The films were deposited at a substrate temperature of 550°C in an Ar [50 standard cubic centimeters per minute (sccm)]/N_2 (5.2 sccm) atmosphere of 9.5 mtorr. The sample-to-target distance was fixed to 4 inches. Before deposition, the vacuum chamber was evacuated until a base pressure of 10^{-7} torr was achieved. X-ray characterization of the samples was performed at room temperature by using a four-circle x-ray diffractometer equipped with Cu-Kα_1 radiation.

HAADF-STEM imaging and atomic-resolution EDS and EELS

Because of the delicate bonding between antiperovskite nitride and perovskite oxide, samples for STEM observation should be carefully prepared. Focused ion beam sampling or prolonged exposure to ion milling caused the interface to collapse, and the damaged area looks dark with a few nanometers thickness along the interface. Therefore, samples were prepared via the conventional way. Samples were mechanically ground to a thickness of less than 50 μm (EM TXP, Leica, Germany), dimpled to a thickness of ~5 μm (Dimple Grinder II, Gatan, USA), and thinned for electron transparency by Ar ion-beam milling with LN_2-cooling stage (Precision Ion Polishing System II, Gatan, USA). HAADF-STEM images were taken in a STEM (JEM-2100F, JEOL) at 120 kV, with a spherical aberration corrector (CEOS GmbH). The optimum size of the electron probe was ~1.2 Å. The collection semi-angles of the HAADF detector were adjusted from 70 to 240 mrad. The obtained raw images were band-pass–filtered to reduce background noise (HREM Filters Pro, HREM research, Japan). To identify the interfacial chemistry, electron-energy-loss spectra were obtained in JEM-2100F (JEOL) at 120 kV using an EEL spectrometer (GIF Quantum ER, Gatan, USA). Because Ga, Sr, Ta, and Al species are not detectable via EELS, the further chemistry at the interface was understood via the atomic-level EDS with a 100-mm^2 detector (X-max^N, Oxford, UK).

Computational details

First-principles calculations were performed with the projector augmented-wave method (*30*) implemented in Vienna Ab initio Simulation Package (*31*) using unconstrained noncollinear magnetic structures (*32*, *33*). The exchange and correlation effects were treated within the generalized gradient approximation (*34*). We used the plane-wave cutoff energy of 550 eV and 16 × 16 × 16 and 12 × 12 × 1 *k*-point meshes in the irreducible Brillouin zone for bulk and interface structures, respectively. Two supercells of $Mn_3GaN/LaAlO_3$ (with the formula $Mn_{12}Ga_4N_5La_4Al_5O_{14}$ for MnN phase and $Mn_{14}Ga_4N_5La_4Al_5O_{14}$ for Mn_2N phase) were used to simulate the interfacial structure (Fig. 5A). Since previous reports showed that magnetism strongly influences the calculated lattice constant in Mn_3GaN (*16*), when optimizing the lattice structure, we assumed a noncollinear magnetic order in bulk Mn_3GaN, while the interfacial MnN layer was set to be antiferromagnetically aligned to the neighboring GaMn layer. The in-plane lattice constant of the interface supercell was constrained to the calculated lattice constant of bulk cubic Mn_3GaN (a = 3.867 Å). The internal coordinates and the c lattice constant were relaxed until the force on each atom was less than 0.001 eV/Å. When evaluating the stability of Mn/ABO_3, we used the symmetric supercells (with the formula $Mn_2A_4B_5O_{14}$) made by an ABO_3 slab, Mn monolayers, and a vacuum layer over 15 Å, as shown in fig. S10.

The formation energies were evaluated as follows (*35*)

$$\Delta E_{\mathrm{MnN\_interface}} = (E_{\mathrm{supercell}} - 4E_{\mathrm{Mn_3GaN}} - 4E_{\mathrm{LaAlO_3}} - E_{\mathrm{Al}} - E_{\mathrm{N}} - 2E_{\mathrm{O}})/2$$

$$\Delta E_{\mathrm{Mn_2N\_interface}} = (E_{\mathrm{supercell}} - 4E_{\mathrm{Mn_3GaN}} - 4E_{\mathrm{LaAlO_3}} - E_{\mathrm{Al}} - E_{\mathrm{N}} - 2E_{\mathrm{O}} - 2E_{\mathrm{Mn}})/2$$

$$\Delta E_{\mathrm{Mn/LaAlO_3}} = (E_{\mathrm{supercell}} - 4E_{\mathrm{LaAlO_3}} - 2E_{\mathrm{Mn}} - E_{\mathrm{Al}} - 2E_{\mathrm{O}})/2$$

where E_{Mn3GaN}, E_{LaAlO3}, E_{B}, and E_{Mn} are the total energies of the related bulk material, and E_{N} and E_{O} are the half of the total energies of the related molecule.

SUPPLEMENTARY MATERIALS

Supplementary material for this article is available at http://advances.sciencemag.org/cgi/content/full/6/30/eaba4017/DC1

REFERENCES AND NOTES

1. J. Mannhart, D. G. Schlom, Oxide interfaces—An opportunity for electronics. *Science* **327**, 1607–1611 (2010).
2. P. Zubko, S. Gariglio, M. Gabay, P. Ghosez, J. M. Triscone, Interface physics in complex oxide heterostructures. *Annu. Rev. Condens. Matter Phys.* **2**, 141–165 (2011).
3. H. Y. Hwang, Y. Iwasa, M. Kawasaki, B. Keimer, N. Nagaosa, Y. Tokura, Emergent phenomena at oxide interfaces. *Nat. Mater.* **11**, 103–113 (2012).
4. J. Chakhalian, A. J. Millis, J. Rondinelli, Whither the oxide interface. *Nat. Mater.* **11**, 92–94 (2012).
5. C. J. Palmstrom, Epitaxy of dissimilar materials. *Annu. Rev. Mater. Sci.* **25**, 389–415 (1995).
6. M. O'Sullivan, J. Hadermann, M. S. Dyer, S. Turner, J. Alaria, T. D. Manning, A. M. Abakumov, J. B. Claridge, M. J. Rosseinsky, Interface control by chemical and dimensional matching in an oxide heterostructure. *Nat. Chem.* **8**, 347–353 (2016).
7. S. V. Krivovichev, Minerals with antiperovskite structure: A review. *Z. Kristallogr.* **223**, 109–113 (2008).
8. T. He, Q. Huang, A. P. Ramirez, Y. Wang, K. A. Regan, N. Rogado, M. A. Hayward, M. K. Haas, J. S. Slusky, K. Inumara, H. W. Zandbergen, N. P. Ong, R. J. Cava, Superconductivity in the non-oxide perovskite $MgCNi_3$. *Nature* **411**, 54–56 (2001).
9. Y. Sun, X. Q. Chen, S. Yunoki, D. Li, Y. Li, New family of three-dimensional topological insulators with antiperovskite structure. *Phys. Rev. Lett.* **105**, 216406 (2010).
10. R. Yu, H. Weng, Z. Fang, X. Dai, X. Hu, Topological node-line semimetal and Dirac semimetal state in antiperovskite Cu_3PdN. *Phys. Rev. Lett.* **115**, 036807 (2015).

11. S. Lin, D. F. Shao, J. C. Lin, L. Zu, X. C. Kan, B. S. Wang, Y. N. Huang, W. H. Song, W. J. Lu, P. Tong, Y. P. Sun, Spin-glass behavior and zero-field-cooled exchange bias in a Cr-based antiperovskite compound $PdNCr_3$. *J. Mater. Chem. C* **3**, 5683–5696 (2015).
12. M. Bilal, S. Jalali-Asadabadi, R. Ahmad, I. Ahmad, Electronic properties of antiperovskite materials from state-of-the-art density functional theory. *J. Chem.* **2015**, 495131 (2015).
13. W. F. Goh, W. E. Pickett, Survey of the class of isovalent antiperovskite alkaline-earth pnictide compounds. *Phys. Rev. B.* **97**, 035202 (2018).
14. D. Matsunami, A. Fujita, K. Takenaka, M. Kano, Giant barocaloric effect enhanced by the frustration of the antiferromagnetic phase in Mn_3GaN. *Nat. Mater.* **14**, 73–78 (2015).
15. T. Peng, W. Bo-Sen, S. Yu-Ping, Mn-based antiperovskite functional materials: Review of research. *Chinese Phys. B.* **22**, 067501 (2013).
16. P. Lukashev, R. F. Sabirianov, K. Belashchenko, Theory of the piezomagnetic effect in Mn-based antiperovskites. *Phys. Rev. B.* **78**, 184414 (2008).
17. P. Lukashev, K. D. Belashchenko, R. F. Sabirianov, Large magnetoelectric effect in ferroelectric/piezomagnetic heterostructures. *Phys. Rev. B.* **84**, 134420 (2011).
18. J. Zemen, E. Mendive-Tapia, Z. Gercsi, R. Banerjee, J. B. Staunton, K. G. Sandeman, Frustrated magnetism and caloric effects in Mn-based antiperovskite nitrides: Ab initio theory. *Phys. Rev. B.* **95**, 184438 (2017).
19. D.-F. Shao, G. Gurung, T. R. Paudel, E. Y. Tsymbal, Electrically reversible magnetization at the antiperovskite/perovskite interface. *Phys. Rev. Mater.* **3**, 024405 (2019).
20. K. Shi, Y. Sun, J. Yan, S. Deng, L. Wang, H. Wu, P. Hu, H. Lu, M. I. Malik, Q. Huang, C. Wang, Baromagnetic effect in antiperovskite $Mn_3Ga_{0.95}N_{0.94}$ by neutron powder diffraction analysis. *Adv. Mater.* **28**, 3761–3767 (2016).
21. E. F. Bertaut, D. Fruchart, J. P. Bouchaud, R. Fruchart, Diffraction neutronique de Mn_3GaN. *Solid State Commun.* **6**, 251–256 (1968).
22. D. Boldrin, A. P. Mihai, B. Zou, J. Zemen, R. Thompson, E. Ware, B. V. Neamtu, L. Ghivelder, B. Esser, D. W. McComb, P. Petrov, L. F. Cohen, Giant piezomagnetism in Mn_3NiN. *ACS Appl. Mater. Interfaces* **10**, 18863–18868 (2018).
23. D. Boldrin, I. Samathrakis, J. Zemen, A. Mihai, B. Zou, F. Johnson, B. D. Esser, D. W. McComb, P. K. Petrov, H. Zhang, L. F. Cohen, Anomalous Hall effect in noncollinear antiferromagnetic Mn_3NiN thin films. *Phys. Rev. Mater.* **3**, 094409 (2019).
24. G. Gurung, D.-F. Shao, T. R. Paudel, E. Y. Tsymbal, Anomalous Hall conductivity of non-collinear magnetic antiperovskites. *Phys. Rev. Mater.* **3**, 044409 (2019).
25. H. Chen, Q. Niu, A. H. Macdonald, Anomalous Hall effect arising from noncollinear antiferromagnetism. *Phys. Rev. Lett.* **112**, 017205 (2014).
26. A. H. MacDonald, M. Tsoi, Antiferromagnetic metal spintronics. *Phil. Trans. R. Soc. A* **369**, 3098–3114 (2011).
27. S. Nakatsuji, N. Kiyohara, T. Higo, Large anomalous Hall effect in a non-collinear antiferromagnet at room temperature. *Nature* **527**, 212–215 (2015).
28. Z. Q. Liu, H. Chen, J. M. Wang, J. H. Liu, K. Wang, Z. X. Feng, H. Yan, X. R. Wang, C. B. Jiang, J. M. D. Coey, A. H. MacDonald, Electrical switching of the topological anomalous Hall effect in a non-collinear antiferromagnet above room temperature. *Nat. Electron.* **1**, 172–177 (2018).
29. T. Jungwirth, J. Sinova, A. Manchon, X. Marti, J. Wunderlich, C. Felser, The multiple directions of antiferromagnetic spintronics. *Nat. Phys.* **14**, 200–203 (2018).
30. P. E. Blöchl, Projector augmented-wave method. *Phys. Rev. B.* **50**, 17953–17979 (1994).
31. D. Joubert, From ultrasoft pseudopotentials to the projector augmented-wave method. *Phys. Rev. B.* **59**, 1758–1775 (1999).
32. D. Hobbs, G. Kresse, J. Hafner, Fully unconstrained noncollinear magnetism within the projector augmented-wave method. *Phys. Rev. B.* **62**, 11556–11570 (2000).
33. D. Hobbs, J. Hafner, D. Spišák, Understanding the complex metallic element Mn. I. Crystalline and noncollinear magnetic structure of α–Mn. *Phys. Rev. B.* **68**, 014407 (2003).
34. J. P. Perdew, K. Burke, M. Ernzerhof, Generalized gradient approximation made simple. *Phys. Rev. Lett.* **77**, 3865–3868 (1996).
35. V. Stevanović, S. Lany, X. Zhang, A. Zunger, Correcting density functional theory for accurate predictions of compound enthalpies of formation: Fitted elemental-phase reference energies. *Phys. Rev. B.* **85**, 115104 (2012).

Acknowledgment

Funding: This work was supported by the NSF under DMREF grant no. DMR-1629270 and the Army Research Office through Grant W911NF-17-1-0462. Transport measurement at the University of Wisconsin-Madison was supported by the U.S. Department of Energy (DOE), Office of Science, Office of Basic Energy Sciences (BES), under award number DE-FG02-06ER46327. S.-Y.C. acknowledges the support of the Global Frontier Hybrid Interface Materials of the National Research Foundation of Korea (NRF) funded by the Ministry of Science and ICT (2013M3A6B1078872) and POSTECH-Samsung Electronics Industry-Academia Cooperative Research Center. Research at University of Nebraska-Lincoln was partly supported by the NSF Materials Research Science and Engineering Center (MRSEC) under grant no. DMR-1420645. K.S acknowledges an NRF grant funded by the Korean government (NRF-2018R1A2B6008258) and the Fundamental Research Program of the Korea Institute of Materials Science (PNK6410). Research at the University of California-Irvine was supported by the Department of Energy (DOE), Office of Research, Office of Basic Science (BES), under grant DE-SC0014430. **Author contributions:** C.-B.E., S.-Y.C., and M.S.R. supervised the experiments. E.Y.T. supervised theoretical calculations. C.X.Q. and T.N. fabricated and characterized thin-film samples. N.C. and M.S.R. carried out electrical transport measurements. K.S. and S.-Y.C. carried out STEM work including the atomic-scale EELS and EDS analyses. L.X. and X.P. carried out the preliminary STEM work. D.-F.S., T.R.P., and E.Y.T. performed theoretical calculations. All authors took part in the analysis. C.X.Q., T.T., S.-Y.C., and C.-B.E. wrote the manuscript. C.-B.E. directed the overall research. **Competing interests:** The authors declare that they have no competing interests. **Data and materials availability:** All data needed to evaluate the conclusions in the paper are present in the paper and/or the Supplementary Materials. Additional data related to this paper may be requested from the authors.

Submitted 30 November 2019
Accepted 10 June 2020
Published 24 July 2020
10.1126/sciadv.aba4017

Citation: C. X. Quintela, K. Song, D.-F. Shao, L. Xie, T. Nan, T. R. Paudel, N. Campbell, X. Pan, T. Tybell, M. S. Rzchowski, E. Y. Tsymbal, S.-Y. Choi, C.-B. Eom, Epitaxial antiperovskite/perovskite heterostructures for materials design. *Sci. Adv.* **6**, eaba4017 (2020).